Supersonic mode in a low-enthalpy hypersonic flow over a cone and wave packet interference

Cite as: Phys. Fluids **33**, 054104 (2021); https://doi.org/10.1063/5.0048089
Submitted: 19 February 2021 . Accepted: 21 April 2021 . Published Online: 13 May 2021

Christopher Haley, and Xiaolin Zhong

Physics of Fluids ARTICLE scitation.org/journal/phf

Supersonic mode in a low-enthalpy hypersonic flow over a cone and wave packet interference

Cite as: Phys. Fluids 33, 054104 (2021); doi: 10.1063/5.0048089
Submitted: 19 February 2021 · Accepted: 21 April 2021 ·
Published Online: 13 May 2021

Christopher Haley[a] and Xiaolin Zhong[b]

AFFILIATIONS

Mechanical and Aerospace Engineering Department, University of California, Los Angeles, California 90095, USA

[a]Author to whom correspondence should be addressed: clhaley@g.ucla.edu
[b]Electronic mail: xiaolin@seas.ucla.edu. URL: http://cfdhost.seas.ucla.edu/

ABSTRACT

A computational fluid dynamics study is conducted in which acoustic-like waves are observed emanating from the boundary layer of a Mach 8 slender blunt cone with a relatively low freestream enthalpy and a warm wall. The acoustic-like wave emissions are qualitatively similar to those attributed to the supersonic mode. However, the supersonic mode responsible for such emissions is often found in high-enthalpy flows with highly cooled walls, making its appearance here unexpected. Linear stability analysis on the steady-state solution reveals an unstable mode S (Mack's second mode) with a subsonic phase velocity and a stable mode F whose mode F- branch takes on a supersonic phase velocity. It is thought that the stable supersonic mode F- is responsible for the acoustic-like wave emissions. Unsteady simulations are carried out using blowing-suction actuators at two different surface locations. The analysis of the temporal data and spectral data using Fourier decomposition reveals constructive/destructive interference occurring between a primary wave packet and a satellite wave packet in the vicinity of the acoustic-like wave emissions. The constructive/destructive interference between the wave packets also appears to have a damping effect on individual frequency growth in both unsteady simulations. Based on this study's results and analysis, it is concluded that a supersonic discrete mode is not limited to high-enthalpy, cold wall flows and that it does appear in low-enthalpy, warm-wall flows; however, the mode is stable.

I. INTRODUCTION

Hypersonic boundary layer transition research is an essential area of investigation because turbulent boundary layers can increase surface heating by a factor of 4–10, which necessitates the application of heavy thermal protection strategies.[1,2] Transition, however, is a process with multiple pathways leading to turbulence, as described by Morkovin *et al.*[3] This paper is concerned with the pathway associated with low environmental forcing, which is typified by discrete normal modes such as the fast and slow modes (modes F and S). These discrete modes are responsible for the well-known Tollmien–Schlichting waves and Mack's second-mode instability, and most recently, by a renewed interest in supersonic modes. Recent research into supersonic modes has shown that unstable supersonic modes can contribute to Mack's second mode and increase the boundary layer's overall instability.[4–6] For this reason, it is important to know under what physical conditions supersonic modes appear and their underlying physical mechanism, which is not currently well understood.

This paper investigates acoustic-like emissions from the boundary layer of a low-enthalpy flow over a Mach 8 cone with a warm-wall condition and an associated wave packet interference pattern between primary and satellite waves. While performing a computational study on surface roughness's ability to attenuate Mack's second-mode instability,[7] the acoustic-like waves seen in Fig. 1 were observed emitting from the boundary layer in an unsteady simulation with no surface roughness. These acoustic-like waves are qualitatively similar to those seen by Chuvakhov and Fedorov,[8] and Knisely and Zhong[5,6,9,10] in their direct numerical simulation (DNS) investigation of supersonic modes. Despite the similarities between the observed phenomena, the simulation conditions are very different; the supersonic mode reliably appears in flows with cooled walls, which makes the appearance of similar acoustic-like waves in a flow with a warm-wall unexpected.

Supersonic modes were first described from Mack's numerical investigations in 1984,[11] 1987,[12] and 1990,[13] and by Reshotko in 1991.[14] Mack showed there exist discrete neutral waves whose phase velocity caused the wave to propagate supersonically relative to the flow at the boundary layer edge, such as when the discrete wave's phase velocity, c, is less than the propagation speed of a slow acoustic wave, $u - a$. In terms of relative Mach number, this relationship is given by

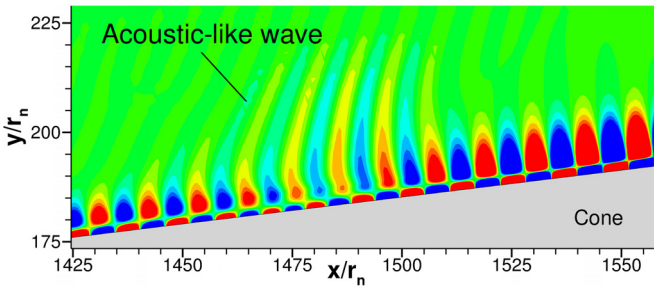

FIG. 1. Weak acoustic-like waves emitting from the boundary layer. The waves are similar in appearance to those emitted by the supersonic mode.

$$\bar{M}(y) = \frac{\bar{u}(y) - c}{\bar{a}(y)} > 1, \tag{1}$$

where $\bar{M}(y)$ is the relative Mach number, $\bar{u}(y)$ is the steady boundary layer velocity, $c = \omega/\alpha$ is the disturbance phase velocity defined by circular frequency ω and streamwise wavenumber α, and $\bar{a}(y)$ is the local steady flow speed of sound.

Mack also showed that supersonic modes transfer energy away from the wall. In unsteady simulations, this property is exhibited as acoustic-like emissions from the boundary layer into the flow behind the bow shock. In Mack's 1987[12] numerical investigation, he found unstable supersonic waves—the instability, however, was much weaker than the second-mode instability and was thus considered less consequential.

Recently, there has been a renewed interest in supersonic modes. Their presence in high-enthalpy impulse facilities motivated Bitter and Shepherd[15] to numerically investigate unstable supersonic modes over cold walls with linear stability theory (LST). They found that decreasing the wall-to-edge temperature ratio leads to unstable supersonic modes appearing over a broader range of frequencies. Their work also characterized an unstable discrete mode (like Mack's second-mode instability) is likely to become supersonically unstable when the complex phase speed has to cross the slow acoustic continuous spectrum.

Shortly thereafter, Chuvakhov and Fedorov performed theoretical and DNS research on unstable supersonic modes where they studied highly cooled plates, with particular attention to the "spontaneous radiation of sound."[8] Their theoretical work showed that Mack's second-mode instability radiates acoustic-like waves out of the boundary layer when synchronized with the slow acoustic continuous spectrum when on a sufficiently cool plate. Tumin also studied the same flow conditions and concluded that the acoustic-like waves are not the result of nonlinear interactions due to nonparallel flow effects and that the boundary layer does have a mechanism for redistributing energy to the inviscid layer.[16]

The effect of nose bluntness on supersonic modes was recently studied by Mortensen.[4] Mortensen's findings show that increasing the nose radius promotes supersonic mode instability and increases the severity of the instability, eventually dominating over the traditional second-mode instability. Knisely and Zhong[5,6] also did an extensive LST and DNS study of supersonic modes in high-enthalpy flows on slender blunt cones with warm and cold walls. A notable result of theirs is that, while they could detect unstable supersonic modes with DNS in both hot and cold wall cases, LST analysis could only detect the supersonic mode in the cold wall case and not the other. They reasoned that this was due to modal interaction and suggested a combined LST and DNS approach to study the supersonic mode. Zanus *et al.*[17] revisited the case of Knisely and Zhong using a combination of LST, linear parabolized stability equations, and DNS. In one warmer wall case, they found the sound radiation came from a stable supersonic mode interacting with the slow acoustic.

Additional theoretical work in the area of supersonic mode instabilities has been done by Wu,[18] and Wu and Zhang,[19] who studied the radiation of supersonic beams emanating from wavetrains. The result is qualitatively similar to the acoustic-like waves seen in unsteady supersonic mode simulations.

The present paper shares some commonalities with the literature already discussed but differs significantly in wall temperature and flow enthalpy. To gain a better idea of where the current case lies in the space of supersonic mode investigations, Fig. 2 compares the total freestream enthalpy and wall-to-recovery temperature ratio of recent investigations with the present investigation. In some instances, the freestream enthalpy and temperature ratios had to be calculated from available parameters. The general trend in Fig. 2 shows that the most recent investigations are highly cooled flows over a range of enthalpies. This is because unstable supersonic modes are reliably known to exist in cooled flows, as Bitter and Shepherd[15] put forth. Figure 2 also shows that the unstable supersonic mode is not highly dependent on the freestream stagnation enthalpy. Low-enthalpy cases with warmer wall conditions were included in the studies done by Chuvakhov and Fedorov,[8] and Mortensen.[4] However, in both instances, no supersonic mode behavior was observed associated with the unstable second mode, and no other modes appear to have been investigated.

The current investigation is far removed from the general trend in Fig. 2, making this paper's in-depth analysis of a low-enthalpy flow with warm-wall condition unique in the literature. Amongst the recent

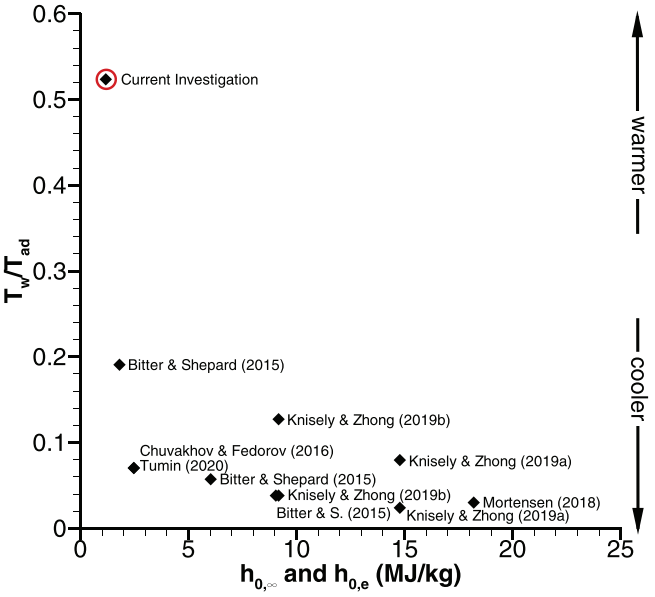

FIG. 2. Comparison of recent supersonic mode investigations and the present investigation by freestream enthalpy and recovery temperature ratio.

supersonic mode investigations, the case parameters in this paper occupy an unexamined space that has been otherwise dismissed because the unstable mode did not have supersonic mode attributes, leaving stable modes unexplored. The current investigation seeks to understand an unexpected numerical result and to shed light on the supersonic mode in low freestream enthalpy flows with a warm-wall condition.

This paper is organized as follows: the governing equations and computational methodology are introduced in Sec. II and followed by the investigation's results in Sec. III. This section is divided into several parts between steady-state flow in III B, the LST analysis in Sec. III C, and the results of two unsteady DNS cases in Sec. III D. A brief description of linear stability theory and relevant details for interpreting the results is provided alongside the LST results in Sec. III C. Likewise, the unsteady simulation methodology is provided with the DNS results in Sec. III D. The final discussion and conclusion are provided in Sec. IV.

II. GOVERNING EQUATIONS AND COMPUTATIONAL METHODOLOGY

This paper uses direct numerical simulation (DNS) of the Navier–Stokes equations to obtain steady and unsteady hypersonic flow solutions over a blunt cone. The DNS code utilizes a unique approach of high-order accurate schemes and shock-fitting to compute the bow shock's location and movement over conical geometries.[20] The blunt cone geometry and high-order shock-fitting approach have been validated extensively for accuracy.

A. Governing equations

The DNS code solves the conservation-law form of the three-dimensional Navier–Stokes equations in Cartesian coordinates. Written in vector form, the governing equations are

$$\frac{\partial U}{\partial t}+\frac{\partial F_j}{\partial x_j}+\frac{\partial G_j}{\partial x_j}=0, \tag{2}$$

in which U is the state vector of conserved quantities, F_j is the inviscid flux vectors, and G_j is the viscous flux vector in the j^{th} spatial direction. The state and flux vectors are defined as

$$U=\{\rho,\ \rho u_1,\ \rho u_2,\ \rho u_3,\ e\}^T, \tag{3}$$

$$F_j=\left\{\rho u_j,\ \rho u_1 u_j+p\delta_{1j},\ \rho u_2 u_j+p\delta_{2j},\ \rho u_3 u_j+p\delta_{3j},\ (e+p)u_j\right\}^T, \tag{4}$$

and

$$G_j=\{0,\ \tau_{1j},\ \tau_{2j},\ \tau_{3j},\ \tau_{jk}u_k-q_j\}^T, \tag{5}$$

where e is internal energy, τ_{ij} is the viscous stress tensor, and q_j is the heat flux. The internal energy, viscous stress, and heat flux, q_j, are defined as follows:

$$e=\rho\left(c_v T+\frac{u_k u_k}{2}\right), \tag{6}$$

$$\tau_{ij}=\mu\left(\frac{\partial u_i}{\partial x_j}+\frac{\partial u_j}{\partial x_i}\right)+\delta_{ij}\lambda\frac{\partial u_k}{\partial x_k}, \tag{7}$$

and

$$q_j=-\kappa\frac{\partial T}{\partial x_j}. \tag{8}$$

Equation (2) is closed assuming a calorically perfect gas

$$p=\rho RT, \tag{9}$$

which is a reasonable assumption for low-enthalpy hypersonic flows. The properties of nitrogen gas are used, which is consistent with the experimental case from which this simulation takes its parameters.[21] The specific heats c_p and c_v are held constant with a given specific heat ratio of $\gamma=1.4$. Meanwhile, a specific gas constant of $R=296.8\,\mathrm{J/kg\,K}$ for nitrogen gas is used, and the viscosity coefficient, μ, is calculated by Sutherland's law in the form

$$\mu=\mu_r\left(\frac{T}{T_o}\right)^{3/2}\frac{T_o+T_s}{T+T_s}, \tag{10}$$

where $\mu_r=1.7894\times10^{-5}\ \mathrm{N\,s/m^2}$, $T_o=288.0$ K, and $T_s=110.33$ K. Finally, the Prandtl number is taken as $-2/3\mu$ and the thermal conductivity, κ, is computed from the constant Prandtl number

$$\kappa=\frac{c_p\mu}{Pr}. \tag{11}$$

Fong and Zhong,[22] Huang and Zhong,[23] and Lei and Zhong[24] have used the same formulation or similar formulations for simulating perfect gas hypersonic flow.

B. Numerical approach

A shock-fitting method is used to obtain an accurate shock location. The shock-fitting method treats the shock as the upper boundary of the physical domain by computing the bow shock's location produced by the blunt cone. Equation (2) is solved in a computational domain with body-fitted curvilinear coordinates (ξ,η,ζ,τ), where ξ is in the direction of the cone surface, η is normal to the cone surface, ζ is in the azimuthal direction, and τ is time. Full transformation details can be found in Ref. 20.

Treating the shock as a domain boundary, the transient shock movement is solved as an ordinary differential equation (ODE) alongside the governing equations. The shock position and speed must be obtained in the form $H(\xi,\zeta,\tau)$ and $H_\tau(\xi,\zeta,\tau)$, and solved as independent flow variables alongside the governing equations. This is accomplished by taking the Rankine–Hugoniot relations, which provide the flow variable boundary conditions behind the shock, as a function of U_∞ and the velocity of the shock front v_n. The shock front velocity is determined by a characteristic compatibility equation at the grid point immediately behind the shock. A complete derivation of H and H_τ can also be found in Ref. 20.

An explicit 5^{th}-order upwind scheme and an explicit 6^{th}-order central finite-difference scheme are used to discretize the inviscid and viscous terms of Eq. (2) in the ξ and η-directions. Second-order derivatives are obtained by applying the schemes twice. Derivatives in the ζ-direction are computed using Fourier collocation. Finally, 5^{th}-order Lax–Friedrichs flux splitting is applied to the inviscid flux terms, and a low storage 3rd-order Runge–Kutta method[25] is used to converge the steady state and to advance the unsteady solutions.

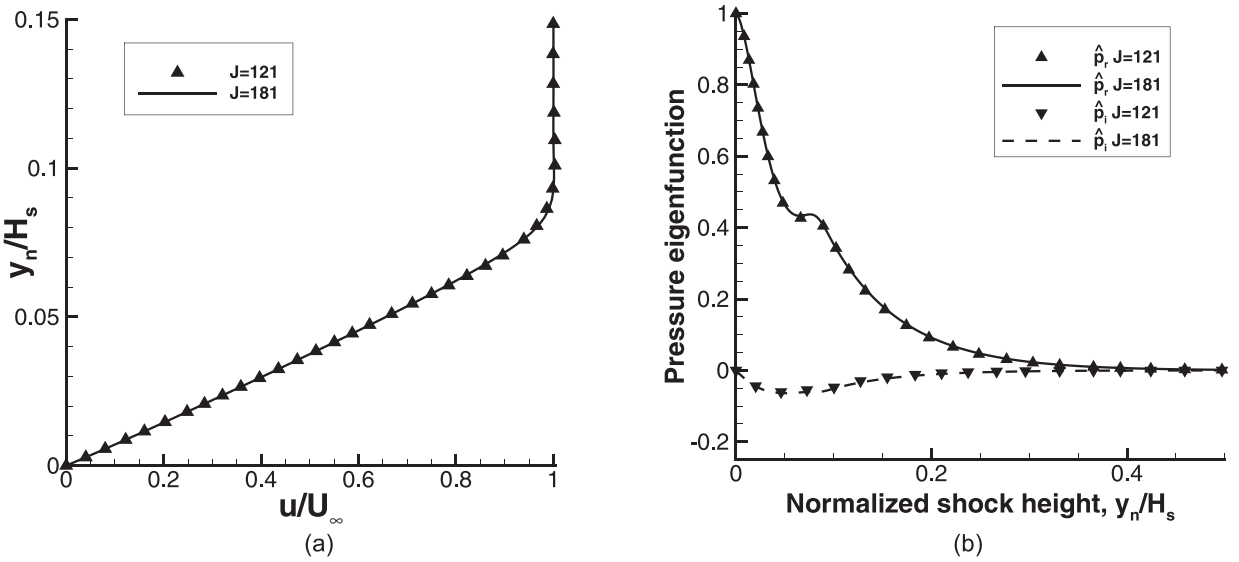

FIG. 3. Steady-state grid independence study of (a) the velocity boundary layer, and (b) the complex pressure perturbation eigenfunction at $s/r_n = 500$ for wall-normal grid distributions J = 121 and 181.

C. Grid independence and convergence

The grid independence study looks at two grid distributions along the cone frustum: a coarse grid of 3602 × 121 points and a fine grid of 7202 × 181 points. Both grid solutions were converged to a relative pressure error of $\mathcal{O}(\varepsilon_p) = 10^{-9}$. Figure 3(a) plots the velocity boundary layer at $s/r_n = 500$ for 121 and 181 points in the wall-normal direction. The profiles are in good agreement for both grid point distributions, indicating an independent solution. The accuracy of the LST stability calculations obtained is also very sensitive to the wall-normal grid distribution of the steady state. The pressure eigenfunction at $s/r_n = 500$ and 160 kHz in Fig. 3(b) also shows there is good agreement between the two grid point distributions. In summary, the solution is converged with no significant differences in the boundary layer profiles or LST eigenfunctions.

III. RESULTS

This paper's simulation approach is to use the aforementioned shock-fitting code to obtain the steady-state solution around a cone. The solution is used as the boundary layer profiles for LST analysis and as the base flow for unsteady DNS simulations. LST provides a theoretical analysis of the discrete boundary layer modes and provides the data required to compute modal phase speeds, growth rates, and eigenfunctions. The unsteady DNS simulation provides a time-accurate evolution of a boundary layer disturbance, which can be analyzed with Fourier decomposition.

A. Simulation conditions

Specifically, the cone geometry in this paper is a slender straight blunt cone at 0° angle-of-attack with a half-angle of 7°, a nose radius of 0.5 mm, and a total length of 1.0 m measured from the nose tip. The flow conditions listed in Table I are taken from a previous experiment[21] performed in Sandia National Laboratories' HWT-8 for the same cone geometry. The freestream conditions are assumed fixed upstream of the bow shock. The shock-fitting algorithm solves the flow field behind the shock and determines its steady-state location. An isothermal wall is assumed along the cone surface from the nose tip to the end of the cone. The isothermal boundary condition neglects surface heating by the flow. Moreover, the wall-to-freestream temperature ratio in Table I is indicative of a warmer wall.

B. Steady-state solution

The steady-state pressure and temperature contours for the cone's blunt nose and frustum are presented together in Fig. 4. Overall, the steady-state solution is typical for a straight blunt cone. Looking at the blunt nose tip in Fig. 4(a), the pressure contours show a maximum pressure ratio at the very tip of the cone, followed by a favorable pressure gradient moving downstream. This favorable pressure gradient quickly gives way to the moderate pressure ratios seen on the frustum in Fig. 4(b). The temperature contours also show a maximum temperature ratio at the nose tip that is offset from the stagnation point due to the isothermal wall boundary condition. Moving to the cone's frustum in Fig. 4(b), the pressure results on the top half of the figure show a moderate pressure ratio and a mildly favorable pressure gradient moving downstream along the cone's length. In the bottom half of Fig. 4(b), the temperature ratio contours show a high

TABLE I. Freestream flow conditions for DNS simulations.

Parameter	Value	Parameter	Value
M_∞	8.0	T_w/T_∞	6.21
ρ_∞	0.024 803 kg/m^3	T_w/T_{ad}	0.52
p_∞	330.743 Pa	T_w	279.0 K
$h_{0,\infty}$	1.174 MJ/kg	Re_∞/l	9 584 257 m^{-1}
U_∞	1093.07 m/s		

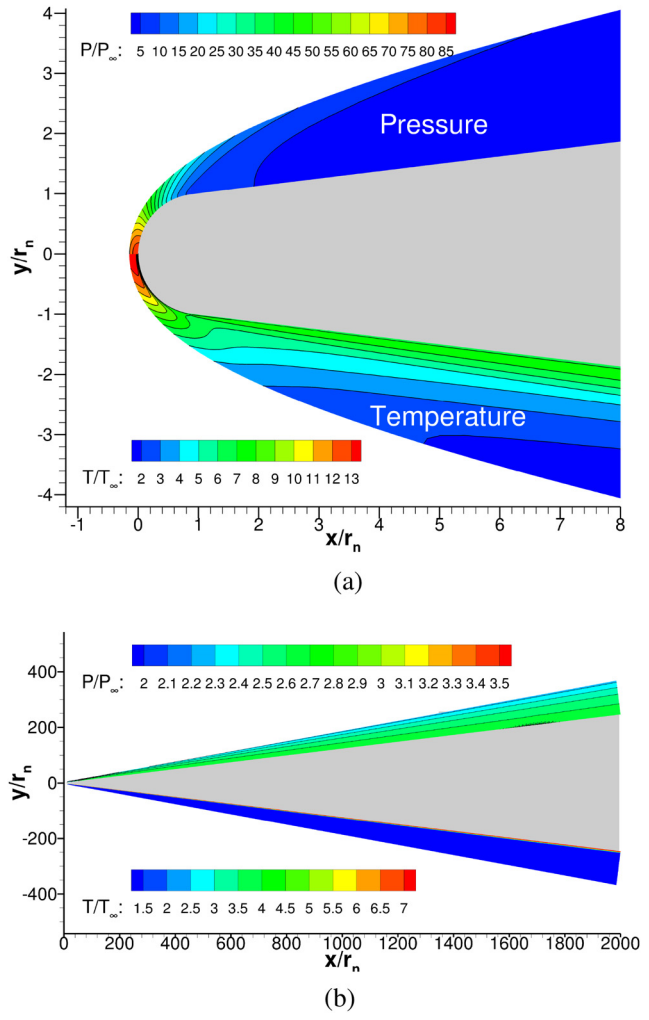

FIG. 4. Pressure and temperature contours at the (a) blunt nose tip, and on the (b) cone frustum. The figures are split with pressure ratio plotted on the top half and temperature ratio plotted on the bottom half.

thermal gradient between the boundary layer and the flow behind the shock, extending over the entire frustum. This high thermal gradient is expected due to the isothermal wall condition, which is considerably higher than the temperature behind the shock and the freestream temperature.

C. Linear stability analysis of steady state

1. Linear stability theory

This paper's linear stability analysis is conducted with a compressible LST code developed by Ma[26,27] following the work done by Malik.[28] To provide a brief overview of LST theory's derivation, the compressible LST equations are obtained from the governing equations, wherein an instantaneous solution comprised of a steady term and a fluctuating term is substituted into Eq. (2). The steady part of the flow is assumed to satisfy Eq. (2) independently and is subtracted from the substitution. Assuming a parallel flow, the remaining steady terms become a function of y only—in practice, the steady-state solution is obtained from the DNS solution and is assumed to be locally parallel. Higher-order fluctuating terms are assumed to be small and are linearized. Finally, a normal mode solution is assumed for the fluctuations of the form

$$q'(y) = \hat{q}(y)\exp\left[i(\alpha x + \beta z - \omega t)\right], \tag{12}$$

where $q'(y)$ is the vector of the fluctuating variables $\{u'(y), v'(y), p'(y), T'(y), w'(y)\}^T$, $\hat{q}(y)$ is the vector of their complex eigenfunctions, α and β are the wavenumbers, and ω is the circular frequency. Substituting the normal mode solution in for the fluctuating terms results in a coupled set of five ordinary differential equations

$$\left(\mathbf{A}\frac{d^2}{dy^2} + \mathbf{B}\frac{d}{dy} + \mathbf{C}\right)\hat{q}(y) = 0, \tag{13}$$

where **A**, **B**, and **C** are complex square matrices and can be found in Ref. 28. Equation (13) constitutes an eigenvalue problem, wherein Dirichlet boundary conditions are applied at the surface and in the far-field. The far-field boundary conditions do not include the bow shock, which is present in the steady-state shock-fitting simulation. For the purposes of this investigation, the shock is considered to be sufficiently far away from the boundary layer as not to have a significant effect on the stability calculations.

The resulting eigenvalue problem is then solved using Malik's multi-domain spectral method approach and a packaged complex eigenvalue solver. The solution of which provides the dispersion relation, Ω, and the complex eigenfunction vector, $\hat{q}$.

The LST equations can be solved using either a temporal stability approach or a spatial stability approach. For the purposes of comparison with DNS, a spatial stability approach is used wherein ω is real, the perturbation is assumed to be 2D ($\beta = 0$), and Eq. (13) is solved for a complex α. The result is a solution to the dispersion relation: $\alpha = \Omega(\omega)$.

In this paper, LST is used to obtain the dispersion relations for the discrete boundary layer modes F and S at select frequencies. The discrete modes' phase speed and growth rate are computed from these LST results. The nondimensional phase speed is defined as

$$c_r = \frac{\omega}{\alpha_r}, \tag{14}$$

where α_r is the real part of the nondimensional wave number. The nondimensional phase speed is used to identify the discrete modes based on where they originate amongst the continuous spectra and interpret their behavior. Likewise, the dimensional growth rate, $-\alpha_i/L^*$, is the negative of the imaginary part of the complex wavenumber over the boundary layer length scale, L^*, where $L^* = \sqrt{s\mu_\infty/\rho_\infty U_\infty}$ and s is the distance along the cone surface. The growth rate is used to identify stable and unstable modes: positive growth rates for unstable modes and negative growth rates for stable modes.

2. Results of linear stability analysis

To study the boundary layer's stability characteristics, LST is used with the steady-state solution to obtain the discrete boundary layer modes F and S. For this particular spatial stability analysis,

160 kHz and 260 kHz are chosen as representative frequencies. As will be seen in Sec. III D, 160 kHz is close to where the constructive/destructive interference behavior occurs, and 260 kHz is in the vicinity of blowing-suction actuators.

Before proceeding, a small discussion on discrete mode terminology is in order. In general, this paper follows the modal naming conventions put forth by Fedorov and Tumin.[29] Mode F describes the discrete modes that originate from the fast acoustic spectrum where $c_r = 1 + 1/M_\infty$, and mode S describes the discrete mode that originates from the slow acoustic spectrum where $c_r = 1 - 1/M_\infty$. If more than one discrete mode appears from either acoustic spectrum, the modes are numbered in order of appearance by increasing ω. Occasionally, a discrete mode may undergo a branch cut or bifurcation when crossing one of the continuous spectra, such as the entropy/vorticity spectrum ($c_r = 1$). In such a case, as ω is increased, the mode approaching the branch cut is given a "+," and the mode departing the branch cut is given a "−." In this paper, mode F undergoes a branch cut when crossing the entropy/vorticity spectrum. In Refs. 5, 15, and 16, however, mode F both crosses a branch cut and bifurcates when crossing the entropy/vorticity spectrum and slow acoustic spectrum, respectively, and "+/−" usage is redefined. These references and this paper use very similar but incongruous discrete mode terminology, so it is important to note that identically named modes may not describe the same physical mode.

The phase speed and growth rate of modes F and S at 160 kHz and 260 kHz are featured in Fig. 5. Figure 5(a) and 5(c) shows how mode F1+ originates in the fast acoustic spectrum and steadily slows down until it reaches the vorticity/entropy branch cut where F1− emerges on the other side. As mode F1−'s phase speed continues to decrease, it couples with mode S, as seen by the mirrored modal growth rate curves in Figs. 5(b) and 5(d). After coupling, mode F1− slows to the slow acoustic wave speed and passes it without coalescing or bifurcating with the slow acoustic branch cut.

Conversely, mode S originates from the slow acoustic spectrum and takes on a phase speed between $c_r = 1$ and $c_r = 1 - 1/M_\infty$. The coupling of mode F1− and mode S causes mode S to become unstable. This is the well-known second-mode instability and is the only unstable mode found in the LST analysis. Furthermore, mode F1− is stable as a consequence of coupling.

Of primary interest to the paper is when any discrete modes become supersonic. This is because the acoustic-like waves seen in Fig. 1 are indicative of a supersonic mode. In addition to the supersonic region within the boundary layer, where $\bar{M} < -1$, there is a second region of relative supersonic flow above it where $\bar{M} > 1$. In order for $\bar{M}$ to be greater than one, the nondimensional phase speed must be less than $1 - 1/M_\infty$. Thus, a discrete mode will be supersonic when $c_r < 1 - 1/M_\infty$.

Of the modes in Fig. 5, only mode F1− is slower than the slow acoustic and becomes supersonic at $\omega = 0.23$. When the phase speed of a discrete mode is supersonic, it is possible for acoustic-like waves to emit into the inviscid region outside of the boundary layer. However, mode F1− is very stable, and any acoustic-like waves are likely to be weak and not sustained without forcing.

By contrast, the supersonic mode in Knisley and Zhong[5,6] and Chuvakhov and Fedorov[8] was an attribute of an unstable F1 mode. Because the mode was unstable, they saw very a strong supersonic response with acoustic-like waves propagating farther outside the boundary layer (see Fig. 9 of Ref. 6 and Figs. 14 and 15 of Ref. 8). Moreover, the unstable supersonic mode F1 had to cross the slow acoustic continuous spectrum branch cut, resulting in a bifurcation of the mode (see Fig. 16 of Ref. 5 and Fig. 4(a) of Ref. 8). There is no similar bifurcation of mode F1− in the present study since its stability keeps it away from the slow acoustic continuous spectrum branch cut as seen in Fig. 6. Thus, any acoustic-like waves produced by the supersonic mode F1− are likely to be damped.

In addition to the LST results, Figs. 5(a) and 5(b) contain phase speed and growth rate results obtained from DNS. The complex wavenumber components needed to compute the phase speed and growth rate are obtained from the amplitude and phase angle of the Fourier decomposed pressure fluctuations at the wall. The wavenumber's real and imaginary parts are computed using the following equations:

$$\alpha_r = \frac{d}{ds}\psi(f), \tag{15}$$

$$\alpha_i = -\frac{1}{\Delta\phi(f)}\frac{d}{ds}\Delta\phi(f), \tag{16}$$

where $\Delta\phi(f)$ is the pressure amplitude-frequency at the wall, and $\psi(f)$ is the phase angle at frequency f. The resulting phase speed and growth rate results consist of the combined discrete and continuous modes. Bi-orthogonal decomposition can be used to extract the discrete modes from the combined signal,[30] but the decomposition is out of scope of the current research. In the meantime, it is possible to gain some insight and comparison between LST and DNS without decomposing the signal further, assuming that the more dominant mode has a more significant influence on the combined signal.

The large oscillations seen in the DNS results in both Figs. 5(a) and 5(b) around $\omega = 0.15$ are attributed to the proximity of the disturbance to the actuator and are attributed to forcing. In general, the DNS phase speed in Fig. 5(a) follows the LST result for mode S; however, it appears translated downward slightly, which could be attributed to influences by mode F1−. It is also important to note that the phase speed dips below $c_r < 1 - 1/M_\infty$ around $\omega = 0.255$, indicating the phase speed becomes supersonic. This supports the idea that the acoustic-like waves seen Fig. 1 and in the unsteady results in Sec. III D result from a supersonic mode. The DNS growth rate in Fig. 5(b) also follows, albeit slightly below, the LST result for mode S, before trending toward the stable growth rate for mode F1−. The DNS phase speed and growth rate trends agree reasonably well with the LST results. The DNS results also support the presence of a supersonic mode.

To better understand how discrete modes can interact with the continuous spectra, the discrete modes featured in Fig. 5 are plotted with the continuous spectra branch cuts in the complex phase speed plane in Fig. 6. The mode's complex phase speed is computed by dividing the mode's frequency by its complex wave number. The real part of the complex phase speed is plotted along the x axis and the imaginary part along the y axis. Demarcations along the top of Fig. 6 denote where discrete modes become supersonic and subsonic based on their nondimensional phase speed. Likewise, divisions along the right side denote where the discrete modes become stable and unstable. In addition to the discrete modes, the figure also includes the branch cuts for the fast acoustic, vorticity/entropy, and slow acoustic continuous spectra. The branch cut locations are calculated using the methods developed by Balakumar and Malik.[31]

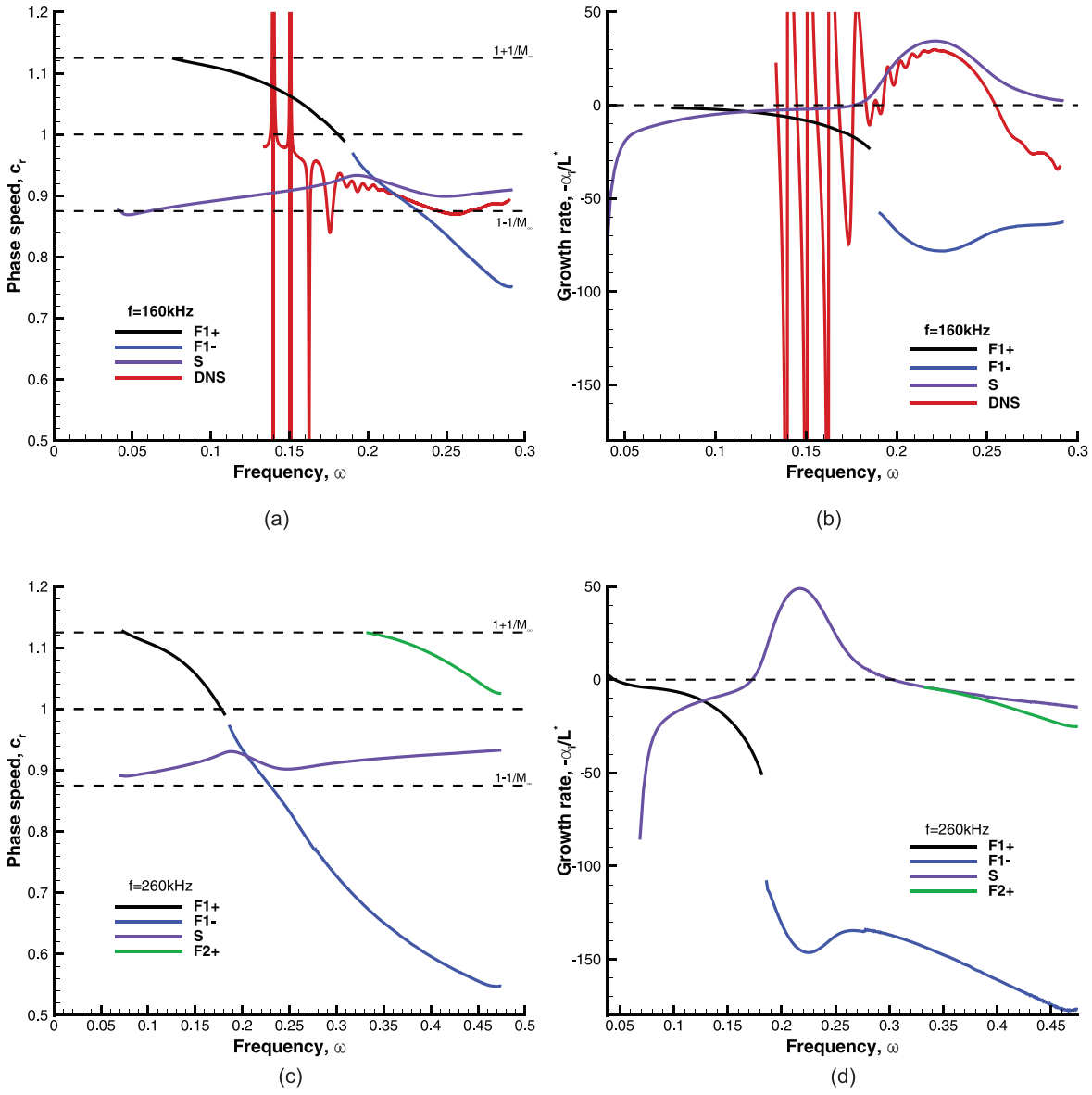

FIG. 5. Nondimensional (a) phase speed and (b) growth rate results for discrete modes F and S at 160 kHz and (c) and (d) 260 kHz, respectively. 160 kHz frequency includes phase speed and growth rate results obtained from unsteady DNS.

Concerning the discrete modes, Fig. 6 shows F1+ originating near the fast acoustic spectrum branch cut on the right side of the figure and then moving left to the vorticity/entropy spectrum branch cut with increasing ω where it stops. From the other side of the vorticity/entropy spectrum branch cut, mode F1− emerges and moves to the left with increasing ω, at one point crossing from a subsonic to supersonic phase speed. Note that both F1+ and F1− are in the stable region of Fig. 6. Mode S originates from the bottom of the figure near the slow acoustic phase speed line and moves upwards toward the unstable region with increasing ω before looping back to the stable region. Unlike mode F, mode S is confined to the subsonic phase speed region.

Similar complex phase speed figures have been plotted by Refs. 8, 9, 15, and 16 in their supersonic mode investigations (see Figs. 4, 16, 10, and 4 of Refs. 8, 9, 15, and 16, respectively). In those investigations, the emergence of a separate discrete supersonic mode was synonymous with a discrete mode coalescing with the slow acoustic spectrum branch cut from above and a separate discrete supersonic mode emerging from below. Thus, the coalescing discrete mode had to have a phase velocity less than $1 - 1/M_\infty$, and an imaginary phase velocity greater than the slow acoustic branch cut, meaning it was both supersonic and unstable. For visual reference, this puts the mode in the upper-left region of Fig. 6. None of the discrete modes

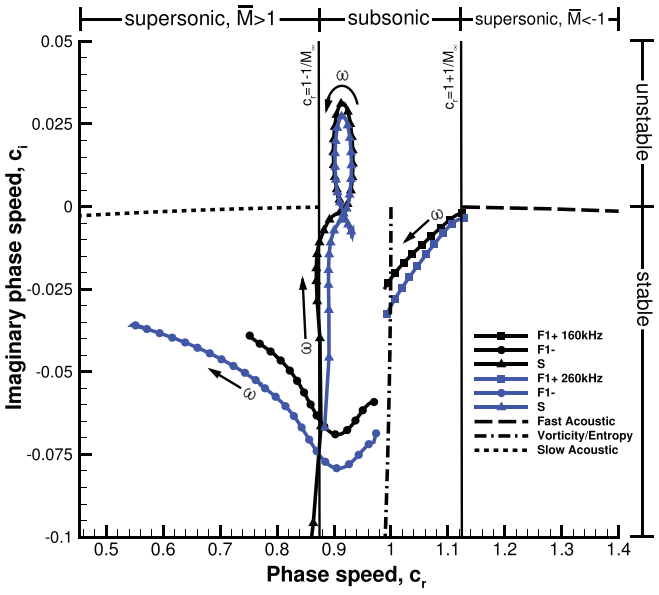

FIG. 6. Discrete modes F and S in the complex phase speed plane for f = 160 and 260 kHz.

investigated by this paper appear in the phase speed plane's upper-left region. LST predicts that the supersonic mode behavior seen in this paper does not appear to result from coalescing or emerging discrete modes. Instead, it results from a stable mode F1−'s decreasing phase speed. By contrast, the coalescing discrete mode in the literature cited above was an unstable mode F1− (according to this paper's mode naming convention). The cited literature also had a very strong acoustic-like wave response, likely due to the mode's instability. However, this is not the case here, where the mode's stability makes the acoustic-like wave response comparatively weak, as seen in the propagating disturbance in Fig. 10. To summarize, the supersonic mode F1− observed in this paper lacks the instability and coalescence with the slow acoustic spectrum branch cut seen in the investigations mentioned above. These differences provide a new view of how supersonic discrete modes behave in low-enthalpy flows with warm-wall conditions.

Moreover, the unstable mode S does not appear to play a role in the observed supersonic behavior unlike the unstable mode in the investigations mentioned above. The loop seen in Fig. 6 is because mode S is multi-valued in c_r due to coupling with F1− (which is monotonic in c_r). Moreover, since mode S generally increases in c_r with increasing ω, it is not likely to cross the slow acoustic wave speed and is therefore not susceptible to supersonic behavior.

Further insight into modes F and S's behavior can be gained by examining the real part of their pressure eigenfunction. In Ref. 5, the supersonic mode's eigenfunction has a strong oscillatory feature that extends outside of the boundary layer. To investigate similar features, this study looks at both mode F1− and S before and after mode F1−'s phase speed crosses the slow acoustic wave speed. Figure 7 contains the eigenfunctions at $\omega = 0.23$, right before mode F1− becomes supersonic, for both modes F1− and S at 160 and 260 kHz. In general, the eigenfunctions' shapes are very similar for both frequencies when

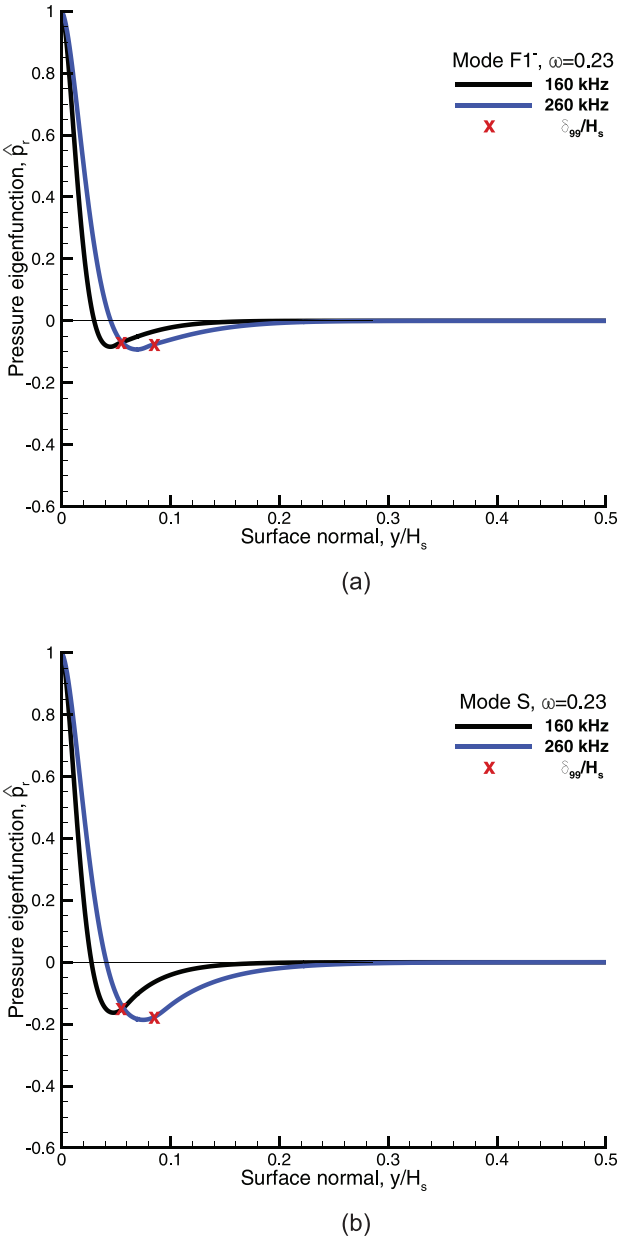

FIG. 7. Comparison of (a) mode F1− and (b) mode S pressure eigenfunctions at $\omega = 0.23$, after synchronization and in the vicinity of the slow acoustic phase speed.

accounting for the growth in the boundary layer and grid stretching in the wall normal direction introduced by normalizing the vertical coordinate, y_n, by the shock height, H_s. The boundary layer edge δ_{99}/H_s is denoted by red x's in each plot; for both mode F1− and mode S, the eigenfunction extends above the boundary layer and does not deviate away from $\hat{p}_r = 0$ once reaching that value in the inviscid layer. Since $\omega = 0.23$ is just before mode F1− becomes supersonic, oscillations into the area behind the shock are not expected for either discrete mode.

Continuing downstream to $\omega = 0.26$ where mode F1−'s phase speed is now supersonic, Fig. 8 contains the plots of the real part of the pressure eigenfunction for both discrete modes at the same frequencies as before. While mode F1−'s phase speed is supersonic, mode S's phase speed is not, thus any oscillations beyond the boundary layer are expected to appear for mode F1− and not mode S. The eigenfunctions are again similar across frequency when controlling for vertical stretching. As before, the profiles extend above the boundary layer edge; however, their shape is slightly different from that seen at $\omega = 0.23$. The mode S profiles are similar, as they do not move away from $\hat{p}_r = 0$ in the inviscid layer. However, the profiles for mode F1− oscillate once about $\hat{p}_r = 0$ above the boundary layer edge before returning to zero, as seen in the inset plot of Fig. 8(a). This oscillation, although weak, is significant because it provides a mechanism for acoustic-like waves to appear in the flow behind the shock. Similarly, unstable supersonic modes produce more persistent oscillations beyond the boundary layer edge (see Fig. 15 of Ref. 5), resulting in the acoustic-like waves seen in the inviscid layer. Furthermore, mode S does not exhibit any oscillations on account of its subsonic phase speed. Thus, it is reasonable to conclude that since mode F1−'s eigenfunction has no oscillations when subsonic and a weak oscillation when supersonic that mode F1− is responsible for the acoustic-like waves seen in the DNS results.

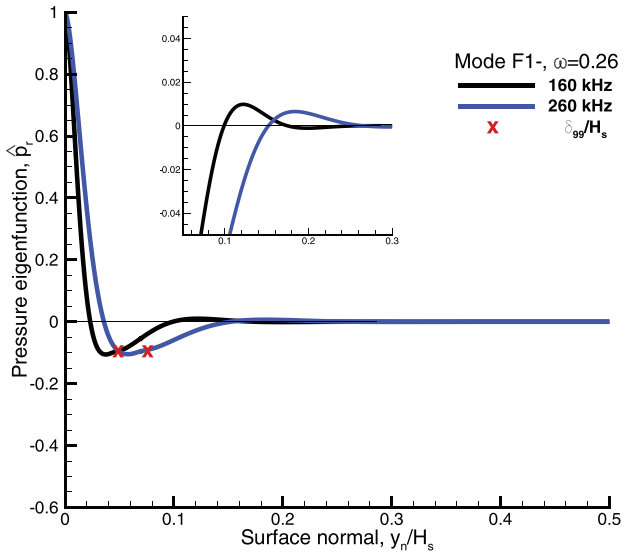

FIG. 8. Comparison of (a) mode F1− and (b) mode S pressure eigenfunctions at $\omega = 0.26$, downstream where mode F1−'s phase speed is less than that of a slow acoustic wave.

An effective way to visualize the supersonic mode using the LST framework is to expand the pressure eigenfunction to produce a contour plot of the pressure fluctuations. An approximate 2D representation of the discrete modes can be obtained using the real part of the normal mode equation used to derive the LST equation

$$p'(y) = Re\{\hat{p}(y)e^{(i(\alpha s-\omega t))}\}, \tag{17}$$

which simplifies to

$$p'(y) = \big(\hat{p}_r(y)\cos(\alpha_r s - \omega t) - \hat{p}_i(y)\sin(\alpha_r s - \omega t)\big)e^{-\alpha_i s}. \tag{18}$$

By substituting the pressure eigenfunction, $\hat{p}$, into Eq. (18), along with its wavenumber, α, and frequency, ω, the pressure perturbation, p', can be obtained at its streamwise location, s. A contour plot of the perturbation is then generated by varying s slightly upstream and downstream, as seen in Fig. 9. The contour levels are normalized by the growth rate term $e^{-\alpha_i s}$ and clipped to visualize the mode better.

The resulting contour plots in Fig. 9 are the normalized pressure fluctuations for modes F1− and S at 160 kHz and $\omega = 0.26$. The local relative Mach number, computed with respect to its discrete mode's phase speed, is plotted on top of the pressure fluctuations as a function of boundary layer height. Dashed lines in each figure demark relative Mach numbers of interest, such as the first sonic line ($\bar{M}(y_{s1}) = -1$), the critical layer ($\bar{M}(y_c) = 0$), and the second sonic line ($\bar{M}(y_{s2}) = 1$). The dashed lines also effectively denote regions in the boundary layer where the relative Mach number is subsonic ($-1 < \bar{M}(y)) < 1$) and supersonic ($\bar{M}(y) > 1$ and $\bar{M}(y) < -1$).

The pressure fluctuation for mode F1− in Fig. 9(a) produces a unique asymmetric repeating pattern. The small oscillation seen in the real part of the eigenfunction in Fig. 8(a), when paired with its imaginary component, actually reveals decaying Mach waves. These Mach waves have a similar appearance to the acoustic-like waves emanating from the boundary layer seen in Fig. 1, albeit smaller in size. Most importantly, these Mach waves also appear above the second sonic line where the relative Mach number is supersonic. When the relative Mach number is greater than 1, the flow is supersonic with respect to the mode's phase speed, signifying that the mode is propagating upstream supersonically in the flow's inertial frame; this is why the Mach waves are angled downstream. Moreover, the Mach waves and second sonic line are consistent with the supersonic mode diagram prepared by Knisely and Zhong for a neutral supersonic mode in the

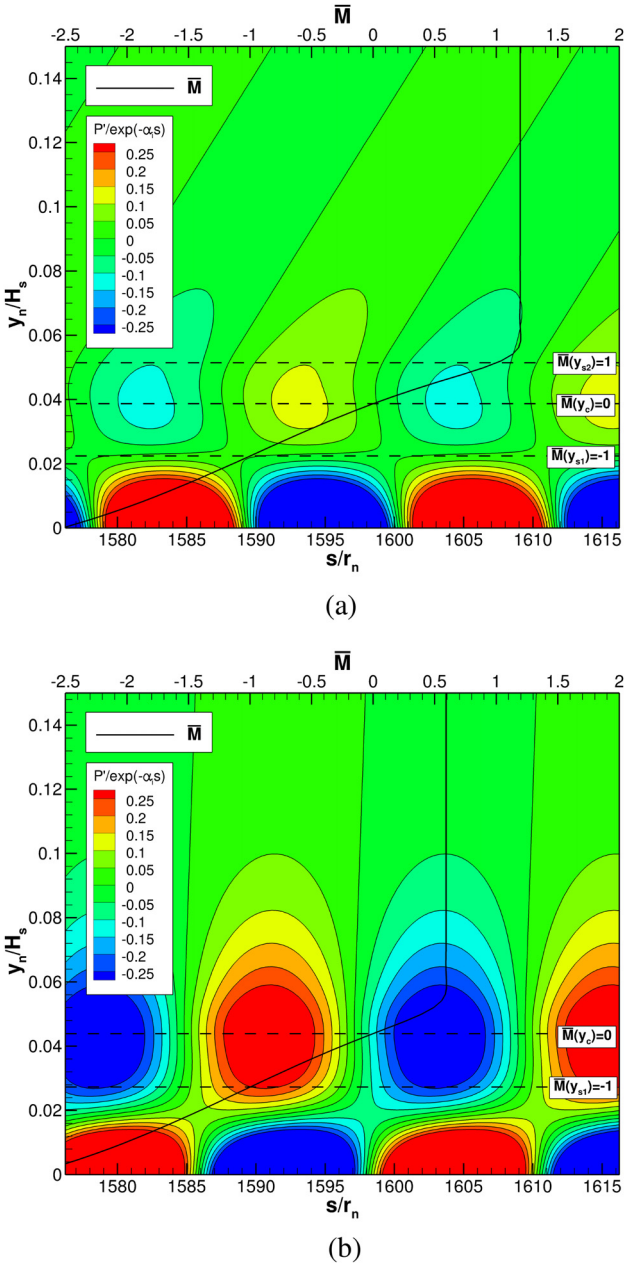

FIG. 9. Normalized pressure fluctuation contours for (a) mode F1− and (b) mode S overlaid with local relative Mach number. Contours are constructed from pressure eigenfunction results obtained from LST at 160 kHz and $\omega = 0.26$. The locations of the first (y_{s2}) and second (y_{s1}) sonic lines and critical layer (yc) are demarcated by relative Mach number.

large wave number limit (see Fig. 2 in Ref. 5). Thus, the appearance of Mach waves above the second sonic line provides further justification that mode F1− is the supersonic mode responsible for the acoustic-like waves.

Unlike mode F1−, the contour of mode S in Fig. 9(b) produces a symmetric repeating pattern of perturbations without decaying Mach waves and has no second sonic line. The absence of these two features is expected because, as shown in Fig. 5(a), mode S is subsonic at $\omega = 0.26$. The relative Mach number profile in Fig. 9(b) confirms this because at no point in the boundary layer is the relative Mach number greater than 1. This is because mode S has a faster wave speed relative to the meanflow than mode F1−. As such, mode S cannot produce Mach waves. Therefore, any supersonic mode behavior observed in the DNS results is due to mode F1− and not mode S.

To summarize, the LST analysis for mode F1− shows that it takes on a supersonic phase speed downstream and has an upper sonic line in the boundary layer when supersonic, and that its eigenfunction produces acoustic-like waves. Therefore, if there exists a supersonic mode in the unsteady simulation, it is likely the result of mode F1−. Similarly, mode S is expected to be subsonic and unstable and not responsible for the observed supersonic behavior.

D. DNS results on a smooth cone

Two unsteady cases are considered in this paper that differ only in the blowing-suction actuator's location. In Case I, the actuator is located at the surface location, $s_c/r_n = 400$, measured from the nose tip, and in Case II at $s_c/r_n = 200$. Initially, the appearance of the primary and satellite waves and acoustic-like waves was observed in Case I. Since the appearance of the acoustic-like waves was unexpected for the present flow conditions, Case II was run to investigate whether the actuator's location was a cause for the unexpected result. The same steady base flow and pulse parameters are used for both DNS cases.

1. Simulation of disturbance

Unsteady disturbances are simulated using a blowing-suction actuator on the cone surface to introduce an unsteady pulse into the steady-state solution flow field. The actuator extends circumferentially around the cone. The pulse has a Gaussian distribution in time and is sinusoidal in space. The sinusoidal shape prevents introducing additional mass into the simulation. The frequency spectrum of the pulse is broad enough to include the most unstable mode frequencies for the given flow conditions. Downstream of the actuator, each frequency is examined for amplification or attenuation based on the frequency spectrum of a temporal Fourier decomposition (FFT). Normalizing each frequency by its initial amplitude makes it possible to compare growth and decay across all frequencies.

The technique of using a Gaussian pulse to examine mode amplification/attenuation was previously implemented by Fong and Zhong[32] and Knisely and Zhong.[5,6] The blowing-suction actuator's mass flux follows the equation:

$$\dot{m}_p(s,t) = \varepsilon(\rho U)_\infty \exp\left(-\frac{(t-\mu)^2}{2\sigma^2}\right)\sin\left(2\pi\frac{s-s_c}{l}\right), \qquad (19)$$

for $s_c < s < s_c + l$ and $t > 0$. In which μ is the mean, σ is the standard deviation, s_c is the actuator's surface location, and l is the length of the actuator. The mass flux is scaled by $\varepsilon(\rho U)_\infty$, where imposing a small ε keeps the flow field's response linear and prevents nonlinear interaction between different frequencies. In this way, the pulse disturbance can be decomposed, and each frequency can be studied independently. The mean of the pulse, μ, is defined in terms of a minimum mass flux, $(\rho v)_{min}$, the initial mass flux at $t = 0$,

TABLE II. Gaussian pulse parameters for DNS.

Parameter	ε	$(\rho v)_{min}$ (kg m/s)	σ (μs)	μ (μs)	x_s (m)	l (mm)
Value	10^{-3}	10^{-10}	0.3	2.0398	0.1976	1.9703

$$\mu = \sqrt{-2\sigma^2 ln\left(\frac{(\rho v)_{min}}{\varepsilon(\rho U)_\infty}\right)}. \tag{20}$$

By defining μ in this way, it can be fixed with a reasonable $(\rho v)_{min}$ regardless of the simulation conditions. The only remaining free parameter in Eq. (19) is the standard deviation, σ, which permits direct control over the pulse's frequency content. The standard deviation in Table II produces a pulse with a nominal spectrum greater than 1 MHz, which is sufficient for the range of unstable mode frequencies found in the unsteady simulation. The remaining pulse parameters used in this paper are given in Table II.

2. Case I: Upstream actuator location

Case I contains the unsteady results that motivated this investigation: the acoustic-like waves emanating from a traveling disturbance. Figure 10 shows acoustic-like waves emanating from the boundary layer as the disturbance develops features of the supersonic mode as it propagates downstream. The acoustic-like waves are relatively weak compared to the overall disturbance strength and do not extend very far into the flow field behind the shock. However, they resemble the supersonic mode and are inconsistent with a pure second-mode instability. The acoustic-like waves are also positioned between a downstream and an upstream portion of the disturbance. As will be shown in Fig. 13, the two portions of the disturbance consist of a primary and satellite wave packet. This brings us to another peculiar aspect of this unsteady disturbance: the periodic constructive/destructive interference between these two packets. As seen in Fig. 10(b), destructive interference creates a "hole" in the oscillation beneath the acoustic-like waves. The hole originates near the surface and does not propagate with the pulse, eventually exiting the disturbance altogether as it propagates downstream. A more detailed look at the interference phenomenon is described in Fig. 11.

The acoustic-like wave emissions and constructive/destructive interference are evident in Fig. 11(a). The downstream angle of the emissions is indicative of their supersonic phase speed as they are propagating supersonically upstream relative to the base flow (albeit translating downstream with the disturbance). The emissions, however, are very weak compared to the much stronger primary wave to its right and the satellite wave to its left. Figure 11(a) shows the disturbance's initial state before any wave interference occurs. In Fig. 11(b), oscillations below the first sonic line, denoted by the arrows A and B, weaken in strength as they start to cancel. Above the first sonic line, the oscillations around $x/r_n = 1500$–1510 begin to interfere, creating a hole with no pressure oscillations. By Fig. 11(c), the weakening oscillations below the sonic line, A and B, have canceled out completely, leaving the oscillations originally to their right and left, A' and B', adjacent to one another. Moreover, the hole appears to exit the disturbance and merge with the disturbance-free pressure field. By Fig. 11(d), the pulse assumes the same appearance as it did in Fig. 11(a) before the wave interference began. In total, the interference pattern appears six times along the cone's length, as the acoustic-like waves emanate uninterrupted from the disturbance.

One way to view the propagation of the disturbance is to plot it as an x-t diagram, such as in Fig. 12, which shows the pressure

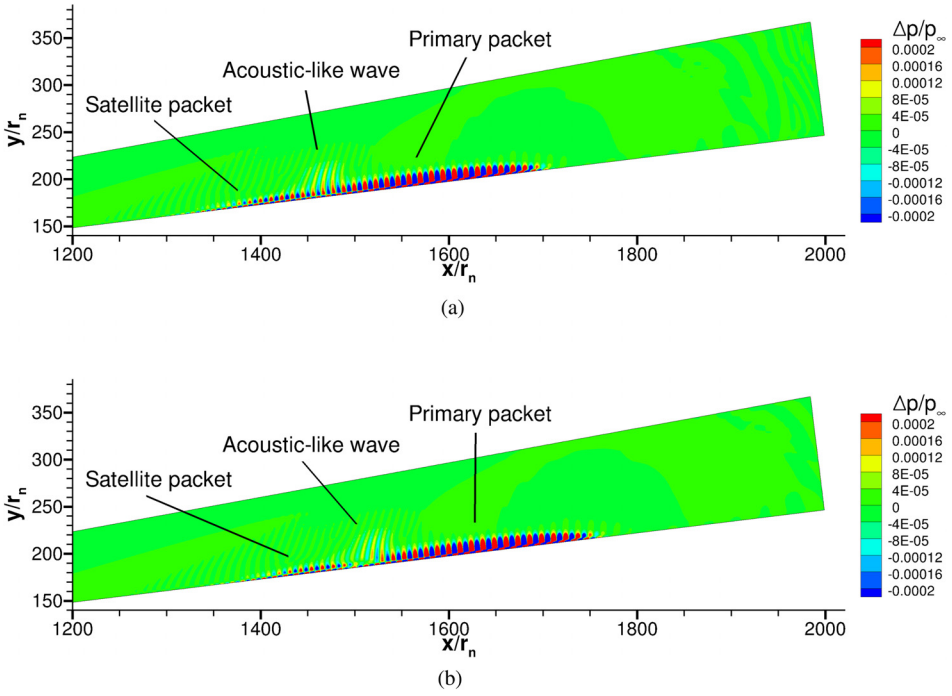

FIG. 10. (a) The acoustic-like waves seen in context of the entire disturbance. (b) A hole in the oscillations develops in the boundary layer beneath the acoustic-like waves due to the destructive interference between the primary and satellite wave packets. The contour levels are clipped to make the pressure perturbations more visible.

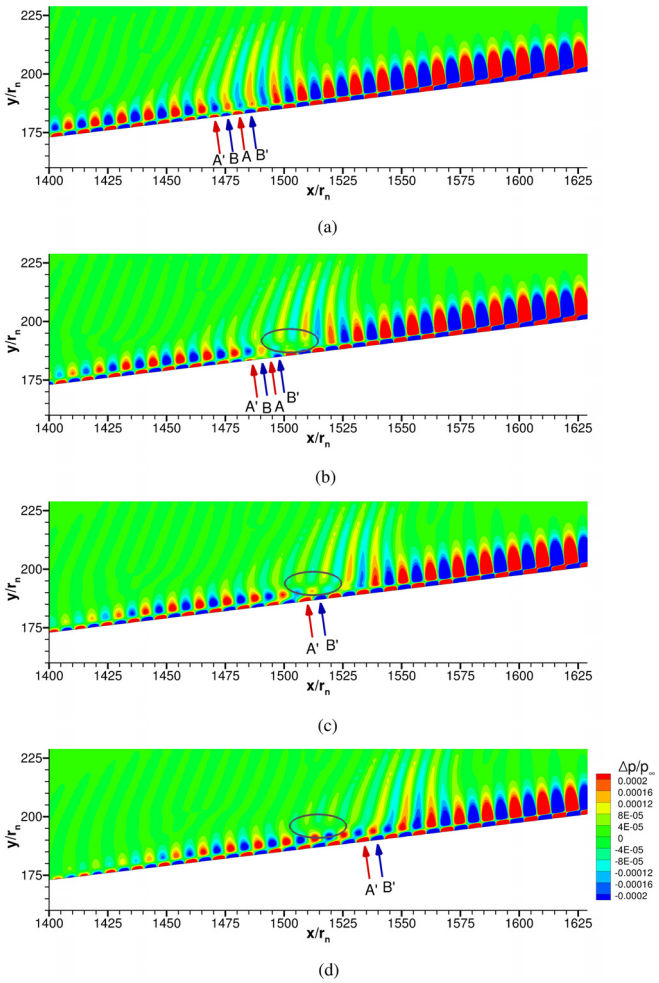

FIG. 11. Progression of pulse interference patterns: (a) wave train prior to interference, (b) interference between oscillations becomes apparent above (ellipse) and below (arrows) the first sonic line, (c) above the sonic line a hole in the oscillations persists into the shock layer, below the sonic line surface oscillations cancel out (arrows A and B), and (d) wave train returns to its previous appearance.

perturbation along the cone's surface over time. An inset plot features the entire unsteady simulation starting from the actuator location at $s_c/r_n = 400$, while the enlarged view features the wave trajectories of the disturbance and several instances of constructive/destructive interference on the cone surface.

The x-t diagram makes it possible to view the individual wave trajectories that makeup the disturbance. From Fig. 12, the leading wave trajectory that comprises the wavefront is present and consistently the same throughout the unsteady simulation—that is, no new wave trajectories appear ahead of it as time progresses, meaning the wavefront propagates steadily downstream. However, the trailing wave trajectory is not the same throughout the simulation. As time progresses, slower wave trajectories appear behind the trailing trajectory, thus becoming the new trailing trajectory and adding to the disturbance's overall width.

Figure 12 shows that as the wave trajectories fan out from the actuator, the primary wave packet comprises the faster shallower

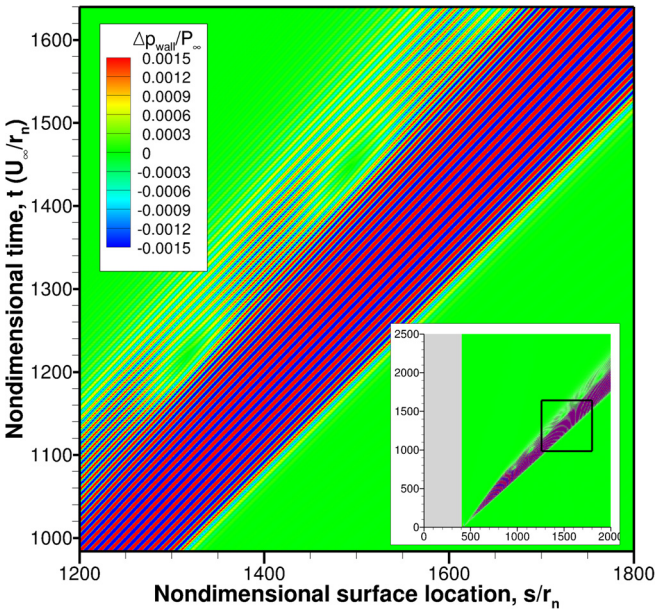

FIG. 12. Case I x-t diagram of unsteady pulse showing the individual wave trajectories. Contours are clipped to show weaker satellite wave; max $|\Delta p_{wall}/P_\infty| = 0.0291$.

trajectories. In contrast, the satellite wave packet, which appears just before the first interference patch, comprises slower, steeper trajectories. As a result of the slower trajectories, the relative Mach number increases across the disturbance from the primary to satellite wave. This is noteworthy because if the relative Mach number across the disturbance becomes greater than one, given appropriate values for flow velocity and speed of sound within the boundary layer, it is possible for the supersonic mode to exist.

Although the x-t diagram provides an entire overview of the unsteady disturbance, it is difficult to discern the disturbance's structure. Figure 13 features time traces along the surface taken at regular nondimensional time intervals, where t has been nondimensionalized by the ratio of the freestream velocity to nose radius, U_∞/r_n. At $t = 328$, the disturbance appears as a single wave packet—this is typical of previous unsteady simulations containing supersonic modes after the actuator's initial forcing.[5] Between $t = 328$ and 682, the disturbance nearly doubles in amplitude. Growth of the disturbance is expected because, as the LST analysis shows, and mode S is unstable. However, its sudden attenuation by $t = 1038$ is atypical and will be discussed at the end of this section. By $t = 682$, however, a satellite wave packet appears as a lower amplitude tail on the main packet. In general, the satellite wave packet can be identified as the packet following the primary wave and by its lower amplitude. When undergoing destructive interference, the two wave packets appear separate from one another; otherwise, the satellite wave packet appears as a long tail connected to the primary wave packet. By $t = 1038$, the satellite wave packet is fully formed, although it is considerably weaker, with $max|\Delta p_{wall}/P_\infty| = 1.33 \times 10^{-3}$ compared to the primary waves at 1.66×10^{-2}. For the intervals between $t = 1038$ and 1749, the satellite wave packet is clearly present and separate from the primary wave.

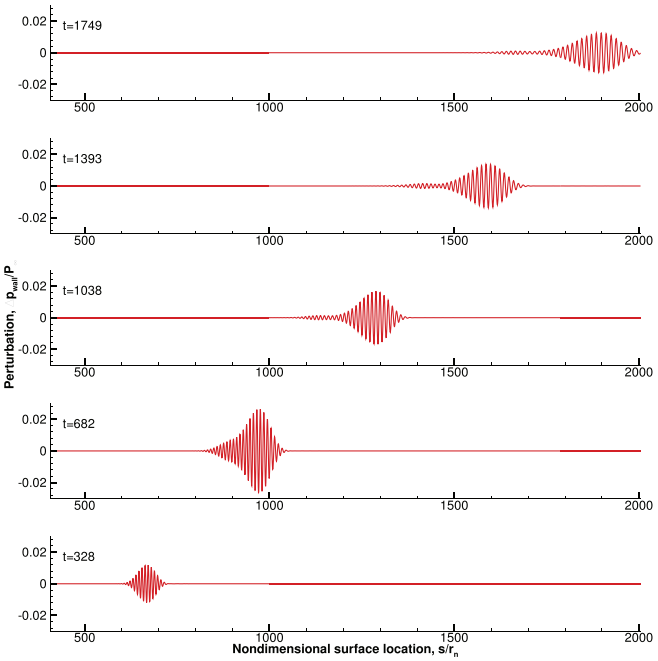

FIG. 13. Propagation of disturbance along the cone surface for Case I with actuator located at $s_c/r_n = 400$. The instantaneous pressure is plotted at five equal nondimensional time intervals of 356.

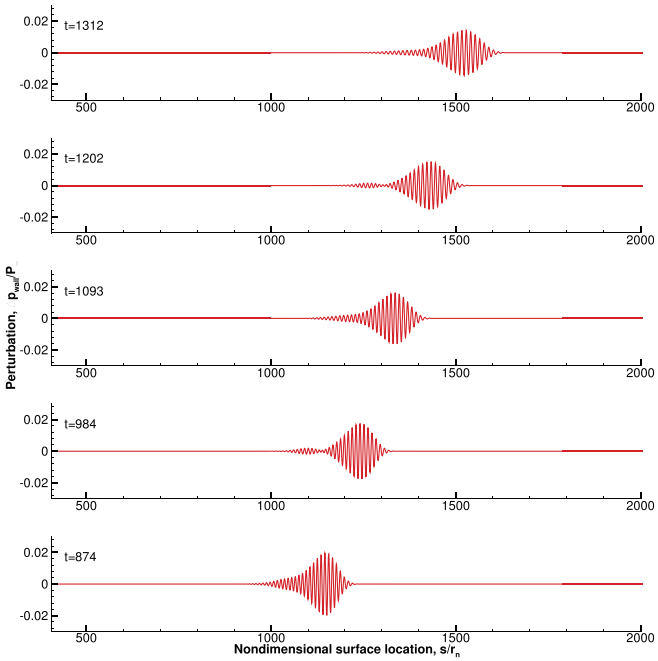

FIG. 14. Case I primary and satellite waves packet evolution over a select time interval. At t = 984 and 1202, both wave packets are distinct from one another due to interference between packets. All other instances show the satellite wave packet as a tail on the primary wave packet. Actuator located at $s_c/r_n = 400$.

A closer look at the interference between the primary and satellite waves is examined in Fig. 14. Whereas Fig. 13 shows the instantaneous propagation of the disturbance over most of the cone, Fig. 14 shows in detail the evolution of the primary and satellite wave packets over a shorter interval. The interval from $t = 874$ and 1312 includes the second and third patches seen in the inset plot of Fig. 12. The satellite wave packet is clearly visible and separate from the primary wave packet at $t = 984$ and 1202, whereas, at $t = 874$, 1093, and 1312, the satellite wave appears as a tail on the primary wave packet.

As the disturbance propagates downstream, it spreads in length due to wave dispersion, as seen in Fig. 12. Since the primary and satellite wave packets are also dispersive, any spreading of the wave packets will cause the waves to interact with one another resulting in either constructive or destructive interference. Constructive and destructive interference occurs when the superposition of two waves forms a resultant wave of greater or lower amplitude. The patches in Fig. 12 and the holes seen in Fig. 11 are likely caused by destructive interference. Likewise, what causes the primary wave and satellite wave to appear attached at $t = 874$, 1093, and 1312 in Fig. 14 results from constructive interference. As was specified previously, the actuator pulse is kept intentionally weak to maintain the disturbance's linear growth and is therefore unlikely to exhibit nonlinear behavior. As such, superposition is a linear process that can account for the repeating pattern of constructive/destructive interference.

How the primary and satellite wave packets relate to the acoustic-like waves is unclear at this point. Except to say that the wave packets are probably the result of forcing by the actuator and that the acoustic-like emissions appear at the interface between primary and satellite wave packets, as seen in Fig. 11.

Since the disturbance is comprised of many different waves, it is possible to use Fourier decomposition to obtain its frequency spectrum. The decomposition is important because it provides insight into the growth and decay of individual frequencies and is more readily compared with LST results. The unsteady wall pressure data featured in Fig. 12 are used to obtain the disturbance's frequency spectrum. The resulting spectrum is normalized by the initial Gaussian pulse in order to compare the growth and decay of individual frequencies together, irrespective of their initial strength. The resulting normalized frequency spectrum is featured in Fig. 15 along with the neutral stability curve for mode S, obtained from LST analysis. There is really good agreement between the spectrum and branch II of the neutral curve. Since growth rates are unstable between branch I and branch II, and stable everywhere else, amplitudes are expected to grow inside the neutral stability curve and decay outside of it. As Fig. 15 shows, the amplitude grows to the left of the branch II neutral stability curve for a fixed frequency and begins to dampen immediately to the right as expected. This result is notable because it shows good agreement between two separate and distinct methods: Fourier decomposition and LST analysis.

An important feature of Fig. 15 is its notable array of peaks and saddles along the perturbed spectrum aligning with the branch II neutral curve. To investigate these peaks and saddles further, fixed frequency slices of the spectrum are plotted in Fig. 16, corresponding to three pairs of peaks and saddles along the perturbed spectrum. Despite the undulations in the frequency spectrum, each frequency still grows and decays in the expected manner—in that there is no modulation within a fixed frequency, only a single peak, indicating that the

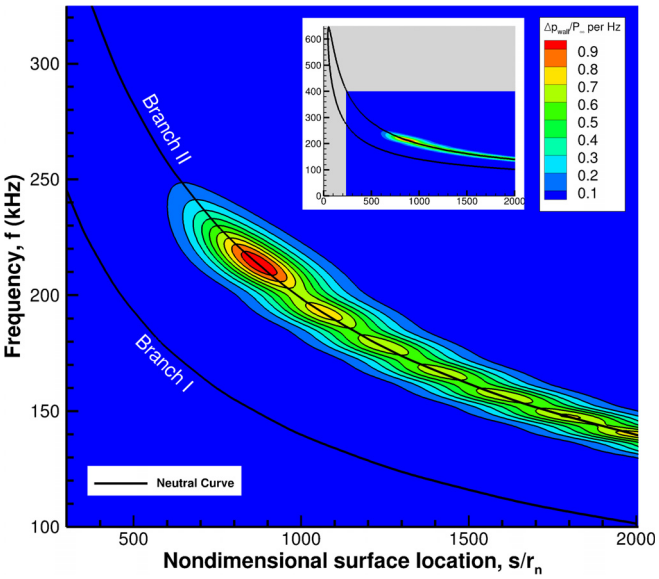

FIG. 15. Case I normalized frequency spectrum of unsteady DNS pressure results combined with unstable mode S neutral stability curve. Actuator located at $s_c/r_n = 400$.

amplitude curves of individual frequencies are more typical than they first appear.

The six patches in Fig. 12 correspond spatially to the six saddles points in Fig. 15, suggesting that the frequencies that undergo destructive interference in the unsteady data are 200, 184, 171, 161, 152, and 143 kHz. As a result of the interference, these frequencies' respective amplitudes are damped. This lends more support to the explanation

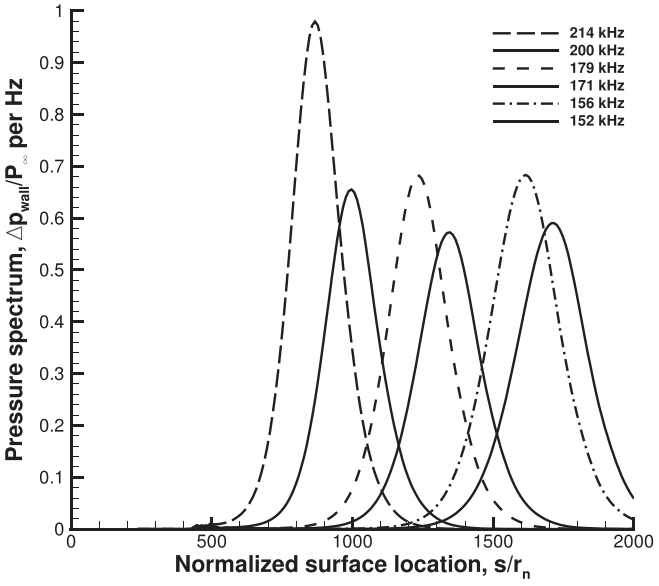

FIG. 16. Case I selected frequencies of the normalized spectrum showing typical growth and decay. Dashed lines correspond to peak frequencies, and solid lines correspond to the nearest saddle point frequency. Actuator located at $s_c/r_n = 400$.

that the patches and holes result from wave superposition, as explained earlier in the paper.

Finally, a note on the atypical growth and attenuation is seen in Fig. 13 around $s/r = 863$. The atypical growth can be attributed to the boundary layer's receptivity at the actuator's location. As seen in Fig. 15, the maximum pressure perturbation corresponds to a frequency of 214 kHz and has neutral stability points at $s/r_n = 403$ and 863. Likewise, the actuator's center, located at $s_c/r_n = 400$, is close to the frequency's branch I neutral point, indicating the boundary layer at the actuator location is highly susceptible to disturbances of 214 kHz. As a result, the atypical growth would appear to be a consequence of the actuator's location and branch I neutral curve. However, the sudden attenuation does not appear to have an apparent cause. As has been suggested in the preceding discussion, destructive interference does provide a means to dampen individual frequencies. Moreover, Tumin's work found that the supersonic mode is a means for redistributing energy from the boundary layer to the inviscid layer.[16] The inference implies that the stable supersonic mode can attenuate boundary layer perturbations; however, detailed analysis is needed to determine the cause of the attenuation.

3. Case II: Upstream actuator location

In addition to Case I, a second unsteady case with a different actuator location is computed. With the unanticipated interference pattern and the unexpected appearance of acoustic-like waves in the first case, it is prudent to investigate whether the actuator's location had any unanticipated forcing on the unsteady results. Undoubtedly, the unsteady results will not be identical to the previous case because moving the actuator's location changes its relationship with the neutral stability curve and its receptivity with the boundary layer. The purpose of this second case is to see whether the same primary and satellite wave packets and the supersonic acoustic-like waves are present. Thus, the actuator is moved upstream to $s_c/r_n = 200$ and run with identical Gaussian pulse parameters as Case I.

Figure 17, like the previous x-t diagram, features the wave trajectories of the complete unsteady disturbance along the cone's surface. An inset plot features the entire unsteady simulation starting from the actuator location at $s_c/r_n = 200$, and the main plot features the wave trajectories of the disturbance and several instances of destructive interference. As in Case I, the leading wave trajectory is the same throughout the unsteady simulation. Moreover, the trailing wave trajectory is also not the same throughout the simulation, with slower wave trajectories appearing behind the trailing trajectory, resulting in an increased disturbance width. The main plot in Fig. 17 also contains the conspicuous interference patches seen in Case I, this time forming a sawtooth-like pattern with the interference patches. These patches are also the result of destructive interference between primary and satellite waves; however, the satellite wave is weaker in this Case.

Examining individual time traces, like those in Fig. 18, reveals that the disturbance's structure is more typical for an unsteady surface pulse: the disturbance grows steadily downstream with little atypical growth and attenuation. From $t = 328$–1749, the maximum amplitude grows 59%, from max $|\Delta p_{wall}/P_\infty| = 5.25 \times 10^{-3}$ to 8.18×10^{-3}. The growth is very mild compared to Case I, which, although having the same initial pulse strength, saw a larger disturbance amplitude. This is likely because the upstream actuator is aligned with the

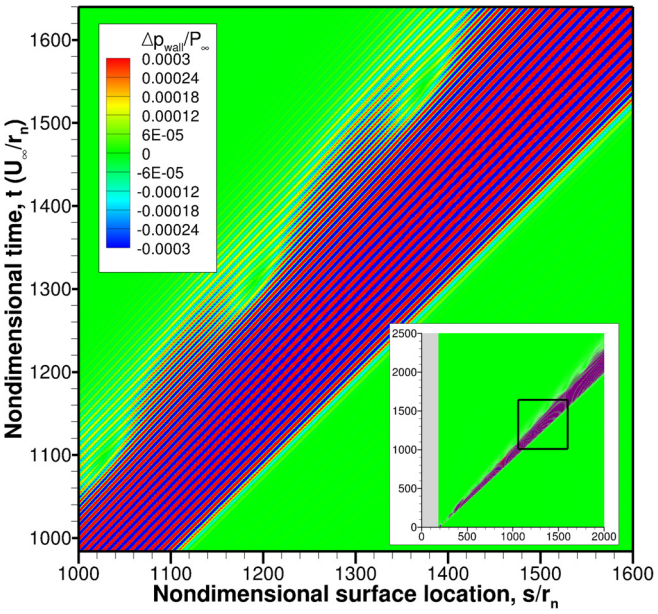

FIG. 17. Case II x-t diagram of unsteady pulse showing individual wave trajectories. Contours are clipped to show weaker satellite wave; max $|\Delta p_{wall}/P_\infty| = 9.37 \times 10^{-3}$.

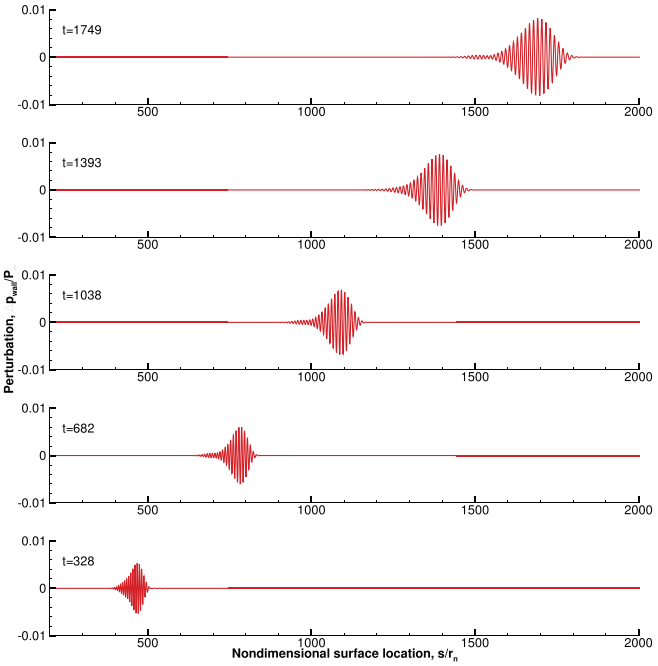

FIG. 18. Case II propagation of disturbance along the cone surface with actuator located at $s_c/r_n = 200$. The instantaneous pressure is plotted at five equal nondimensional time intervals of 355.

narrower, high-frequency portion of the neutral stability curve, as seen in Fig. 19. This means that there will be more damping of the lower frequencies before reaching the neutral curve's unstable region. Regardless of the reduced growth, a satellite wave is present as a tail on the primary wave and is even less prominent than the satellite wave in Fig. 13. This verifies in part that the primary and satellite wave packets and any resulting interference are independent of actuator location.

As before, a Fourier decomposition of the temporal data are used to compute its frequency spectrum. Figure 19 contains both the frequency spectrum and neutral curve for the upstream actuator. Once again, the DNS frequency spectrum agrees very well with the LST neutral curve. Overall, the spectrum increases downstream with decreasing frequency as expected. There is, however, an obvious meandering of the contours. This appears to be a result of the constructive/destructive interference seen in Fig. 17; however, because the satellite wave is much weaker, the same peaks and saddles do not appear in the contour plot as they do in Fig. 15.

Close inspection of the frequency spectrum data, however, does reveal that the meandering contours in Fig. 19 are the result of the same peaks and saddles. Three pairs of fixed frequency peaks and saddles along the perturbed spectrum are plotted in Fig. 20. Like Case I, each frequency grows to a maximum amplitude and decays as anticipated. However, unlike Case I, the perturbed spectrum appears to grow steadily downstream: successive peaks growing higher in amplitude, despite the interspersed saddles. Moreover, the destructive interference between wave packets also appears to have a slight damping effect on the saddle point frequencies, as seen in Case I.

Overall, the Case II unsteady results better resemble the linear disturbance growth expected when using a surface blowing-suction actuator. Even so, the same primary and satellite wave packets, the same acoustic-like emissions, and the same peaks and saddles that appeared in Case I also appear here. Therefore, it is reasonable to conclude that, while the unsteady results did differ, the observed phenomenon of supersonic acoustic-like waves and interference patterns is not solely due to the actuator's placement.

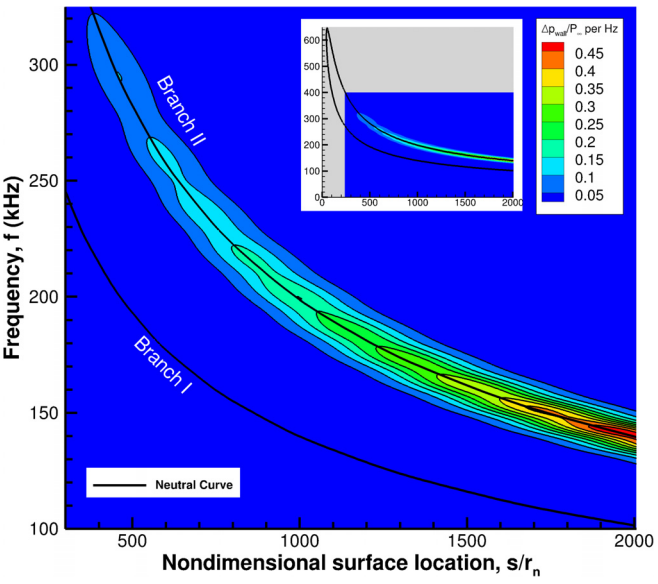

FIG. 19. Case II normalized pressure frequency spectrum of unsteady DNS results combined with unstable mode S neutral stability curve. Actuator located at $s_c/r_n = 200$.

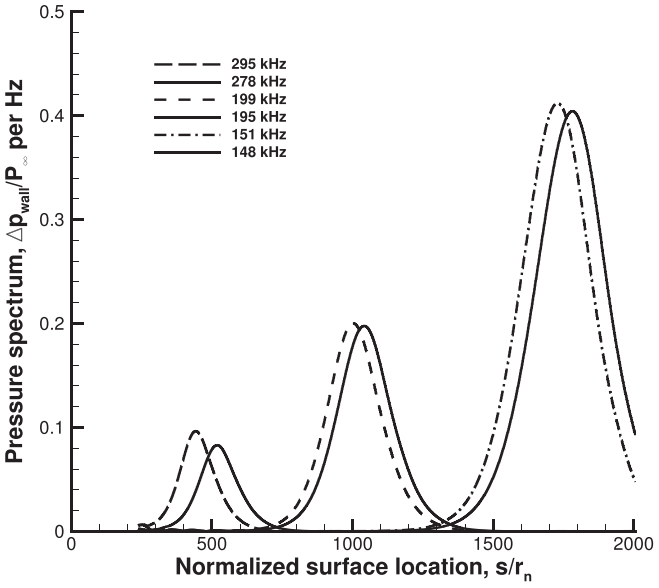

FIG. 20. Case II selected frequencies of the normalized spectrum showing typical growth and decay. Dashed lines correspond to peak frequencies, and solid lines correspond to the nearest saddle point frequency. Actuator located at $s_c/r_n = 200$.

IV. DISCUSSION AND CONCLUSIONS

In this paper, LST and DNS were used to study the propagation of an unsteady disturbance on a cone surface in Mach 8 flow with low freestream enthalpy and a warm-wall condition. The unsteady disturbance exhibited weak acoustic-like waves emanating from the boundary layer and a peculiar constructive/destructive interference pattern. The acoustic-like waves were reminiscent of supersonic discrete modes, which are not expected in low-enthalpy, warm-wall flows. Because of this, the unsteady results merited further investigation.

The origin of the acoustic-like waves appears to result from a supersonic mode as initially predicted. The discrete modes' phase speeds show that modes F1+ and S are both subsonic; only mode F1− acquires a supersonic phase speed after initially being subsonic. A comparison of mode F1−'s eigenfunction before and after becoming supersonic shows the eigenfunction does acquire an additional oscillation when supersonic. A contour plot of the pressure fluctuation generated from the eigenfunction result shows that mode F1− does have angled Mach waves similar to those found in the unsteady simulation. The F1− growth rate results show that the mode is also very stable, resulting in acoustic-like waves that are much weaker than the overall disturbance. Mode F1−'s complex phase speed also shows that it behaves quite differently from other unstable supersonic modes investigated in the literature due to its stability. Where other modes might start unstable, become supersonic, eventually coalesce with the slow acoustic continuous spectrum, and then bifurcate into a separate stable supersonic mode, the supersonic mode in this study starts and remains stable, and becomes supersonic due to decreasing phase speed, never approaching the slow acoustic continuous spectrum. Thus, this study has shown that there is more than one supersonic mode to evolution.

In addition to the LST analysis supporting mode F1− as the supersonic mode, the phase speed of the disturbance computed from DNS data does become momentarily supersonic, further supporting the conclusion that the acoustic-like waves initially motivating this investigation are due to a supersonic mode.

Regarding the unsteady interference pattern, wave trajectories and time traces of unsteady pressure data show clear evidence of constructive/destructive interference between primary and secondary wave packets inside the unsteady disturbance. Fourier decomposition of the unsteady pressure data also shows repeating peaks and saddles in the frequency spectrum that align spatially with the unsteady data's destructive interference pattern. DNS analysis of the results supports the explanation that the pattern results from wave packets trailing one another, while wave dispersion causes them to spread and superimpose with one another resulting in interference. The destructive interference also causes narrow bands of frequencies to dampen in amplitude.

On a methodological note, the reason for using a Gaussian pulse in unsteady simulations is to perturb the boundary layer to a wide range of frequencies and to study the resulting linear modal growth and decay. Understanding what caused the primary and secondary wave packets and peculiar disturbance behavior is vital because it presents an obstacle to researchers whose DNS studies require a coherent wave packet to study linear modal growth. The present investigation supposes this behavior due to the actuator's location and its proximity to the second-mode neutral curve.

In conclusion, supersonic modes are not limited to high-enthalpy, cold-wall flows. Previous studies focused almost exclusively on cool-walled flows for their ability to produce an unstable supersonic discrete mode. This paper demonstrates with LST analysis and DNS results that stable supersonic discrete modes can also exist in warm-walled flows. The LST results show a stable supersonic mode that produces weak Mach waves outside the boundary layer. Likewise, the DNS results show that the supersonic mode can appear in unsteady disturbances with forcing. This paper's new findings indicate that a stable supersonic discrete mode can exist in low-enthalpy, warm-wall flows. This new result contributes to our fundamental knowledge of the supersonic modes' properties and behaviors.

ACKNOWLEDGMENTS

This research was sponsored in part by the Air Force Office of Scientific Research (AFOSR) under Grant No. FA9550–19-1–0206, monitored previously by Dr. Ivett Leyva and presently by Dr. Sarah H. Popkin, and by the Office of Naval Research (ONR) Grant No. N00014–17-1–23-43, monitored by Dr. Eric Marineau. Computational resources were provided by the United States Department of Defense High Performance Computing Modernization Program (DoD HPCMP). Additional computational resources were also provided by the Extreme Science and Engineering Discovery Environment (XSEDE) under Grant No. TG-ASC090076 supported by National Science Foundation. The views and conclusions contained herein are those of the authors and should not be interpreted as necessarily representing the official policies or endorsements either expressed or implied by the AFOSR, the ONR, or the U.S. Government.

DATA AVAILABILITY

The data that support the findings of this study are available from the corresponding author upon reasonable request.

REFERENCES

[1]B. Hollis, "Blunt-body entry vehicle aerothermodynamic: Transition and turbulent heating," J. Spacecr. Rockets **49**, 435–449 (2012).
[2]X. Zhong and X. Wang, "Direct numerical simulation on the receptivity, instability, and transition of hypersonic boundary layers," Annu. Rev. Fluid Mech. **44**, 527–561 (2012).
[3]M. V. Morkovin, E. Reshotko, and T. Herbert, "Transition in open flow systems–A reassessment," Bull. Am. Phys. Soc. **39**, 1882 (1994).
[4]C. Mortensen, "Toward and understanding of supersonic modes in boundary-layer transition for hypersonic flow over blunt cones," J. Fluid Mech. **846**, 789–814 (2018).
[5]C. P. Knisely and X. Zhong, "Sound radiation by supersonic unstable modes in hypersonic blunt cone boundary layers. I. Linear stability theory," Phys. Fluids **31**, 024103 (2019).
[6]C. P. Knisely and X. Zhong, "Sound radiation by supersonic unstable modes in hypersonic blunt cone boundary layers. II. Direct numerical simulation," Phys. Fluids **31**, 024104 (2019).
[7]C. L. Haley and X. Zhong, "Direct numerical simulation of hypersonic flow over a blunt cone with axisymmetric isolated roughness," AIAA Paper No. 2017–4514, 2017.
[8]P. V. Chuvakhov and A. V. Fedorov, "Spontaneous radiation of sound by instability of a highly cooled hypersonic boundary layer," J. Fluid Mech. **805**, 188–206 (2016).
[9]C. P. Knisely and X. Zhong, "Signigicant supersonic modes and the wall temperature effect in hypersonic boundary layers," AIAA J. **57**, 1552–1566 (2019).
[10]C. P. Knisely and X. Zhong, "Impact of vibrational nonequilibrium on the supersonic mode in hypersonic boundary layers," AIAA J. **58**, 1704–1714 (2020).
[11]L. M. Mack, "Boundary layer linear stability theory," AGARD Technical Report No. 709, 1984.
[12]L. Mack, "Review of linear compressible stability theory," in *Stability of Time Dependent and Spatially Varying Flows*, edited by D. Dwoyer and M. Hussaini (Springer-Verlag, 1987), pp. 164–187.
[13]L. M. Mack, "On the inviscid acoustic-mode instability of supersonic shear flows. Part 1: Two-dimensional waves," Theor. Comput. Fluid Dyn. **2**, 97–123 (1990).
[14]E. Reshotko, "Hypersonic stability and transition," in *Hypersonic Flows for Reentry Problems* (Springer-Verlag, Berlin, 1991), Vol. 1, pp. 18–34.
[15]N. Bitter and J. E. Shepherd, "Stability of highly cooled hypervelocity boundary layers," J. Fluid Mech. **778**, 586–620 (2015).
[16]A. Tumin, "Wave packets and supersonic second modes in a high-speed boundary layer," AIAA Paper No. 2020–0106, 2020.
[17]L. Zanus, C. P. Knisely, F. M. Miro, and F. Pinna, "Multiple-tool stability analysis of supersonic modes in thermo-chemical nonequilibrium boundary layers,"AIAA Paper No. 2020–3067, 2020.
[18]X. Wu, "Mach wave radiation of nonlinearly evolving supersonic instability modes in shear layers," J. Fluid Mech. **523**, 121–159 (2005).
[19]X. Wu and Z. Zhang, "First-principle description of acoustic radiation of shear flows," Philos. Trans. R. Soc., A **377**, 20190077 (2019).
[20]X. Zhong, "High-order finite-difference schemes for numerical simulation of hypersonic boundary-layer transition," J. Comput. Phys. **144**, 662–709 (1998).
[21]K. M. Casper, S. J. Beresh, J. F. Henfling, R. W. Spillers, B. O. M. Pruett, and S. P. Schneider, "Hypersonic wind-tunnel measurements of boundary-layer transition on a slender cone," AIAA J. **54**, 1250–1263 (2016).
[22]K. D. Fong, X. Wang, and X. Zhong, "Numerical simulation of roughness effect on the stability of a hypersonic boundary layer," Comput. Fluids **96**, 350–367 (2014).
[23]Y. Huang and X. Zhong, "Numerical study of hypersonic boundary-layer receptivity with freestream hotspot perturbations," AIAA J. **52**, 2652 (2014).
[24]J. Lei and X. Zhong, "Linear stability analysis of nose bluntness effects on hypersonic boundary layer transition," J. Spacecr. Rockets **49**, 24–37 (2012).
[25]J. Williamson, "Low-storage Runge–Kutta schemes," J. Comput. Phys. **35**, 48–56 (1980).
[26]Y. Ma and X. Zhong, "Receptivity of a supersonic boundary layer over a flat plate. Part 1. Wave structures and interactions," J. Fluid Mech. **488**, 31–78 (2003).
[27]Y. Ma and X. Zhong, "Receptivity of a supersonic boundary layer over a flat plate. Part 2. Receptivity to free-stream sound," J. Fluid Mech. **488**, 79–121 (2003).
[28]M. R. Malik, "Numerical methods for hypersonic boundary layer stability," J. Comput. Phys. **86**, 376–413 (1990).
[29]A. Fedorov and A. Tumin, "High-speed boundary-layer instability: old terminology and a new framework," AIAA J. **49**, 1647–1657 (2011).
[30]A. Tumin, "Multimode decomposition of spatially growing perturbations in a two-dimensional boundary layer," Phys. Fluids **15**, 2525 (2003).
[31]P. Balakumar and M. R. Malik, "Discrete modes and continuous spectra in supersonic boundary layers," J. Fluid Mech. **239**, 631–656 (1992).
[32]D. Fong, X. Wang, and X. Zhong, "Finite roughness effect on modal growth of a hypersonic boundary layer," AIAA Paper No. 2012–1086, 2012.